Supplementary Information

Multiple stages of metal exsolution with particle shape governed by proximity to the perovskite surface

Andreas Rosnes[1,*], Bo Jiang[2], Phuong D. Nguyen[1], Luyang Wang[2], Holger von Wenckstern[1], Øystein Prytz[1], Jonathan M. Polfus[2,*]

[1] Department of Physics, Centre for Materials Science and Nanotechnology, University of Oslo, PO Box 1048 Blindern, NO NO-0316 Oslo, Norway

[2] Department of Chemistry, Centre for Materials Science and Nanotechnology, University of Oslo, PO Box 1033 Blindern, NO-0315 Oslo, Norway

* Corresponding authors E-mail: andreas.rosnes@smn.uio.no, jonathan.polfus@kjemi.uio.no

Contents

1. Structure characterization and refinement (XRD)

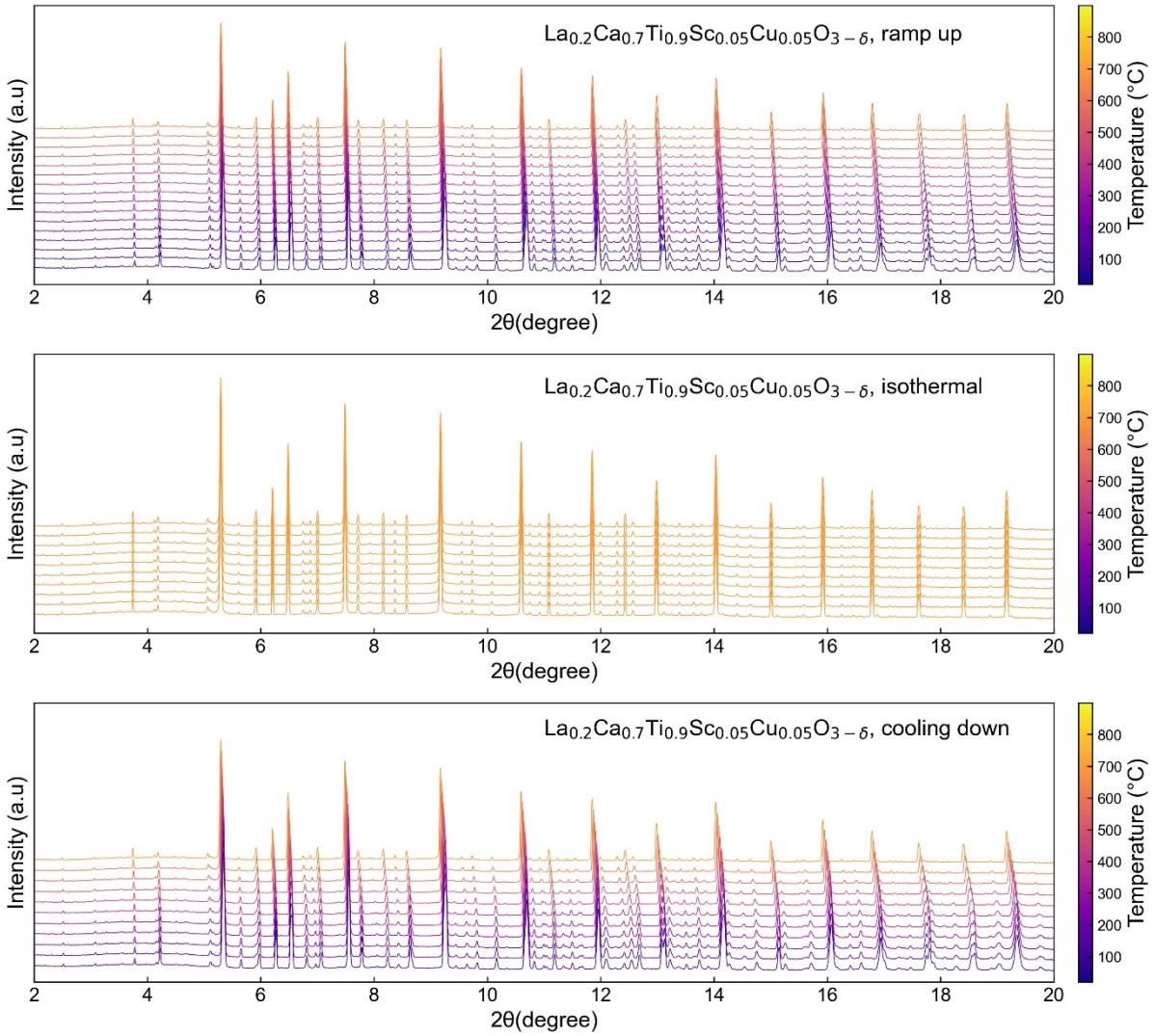

Figure S1.1. Stacked temperature-dependent XRD patterns on logarithmic scale for $La_{0.2}Ca_{0.7}Ti_{0.9}Sc_{0.05}Cu_{0.05}O_{3-\delta}$.

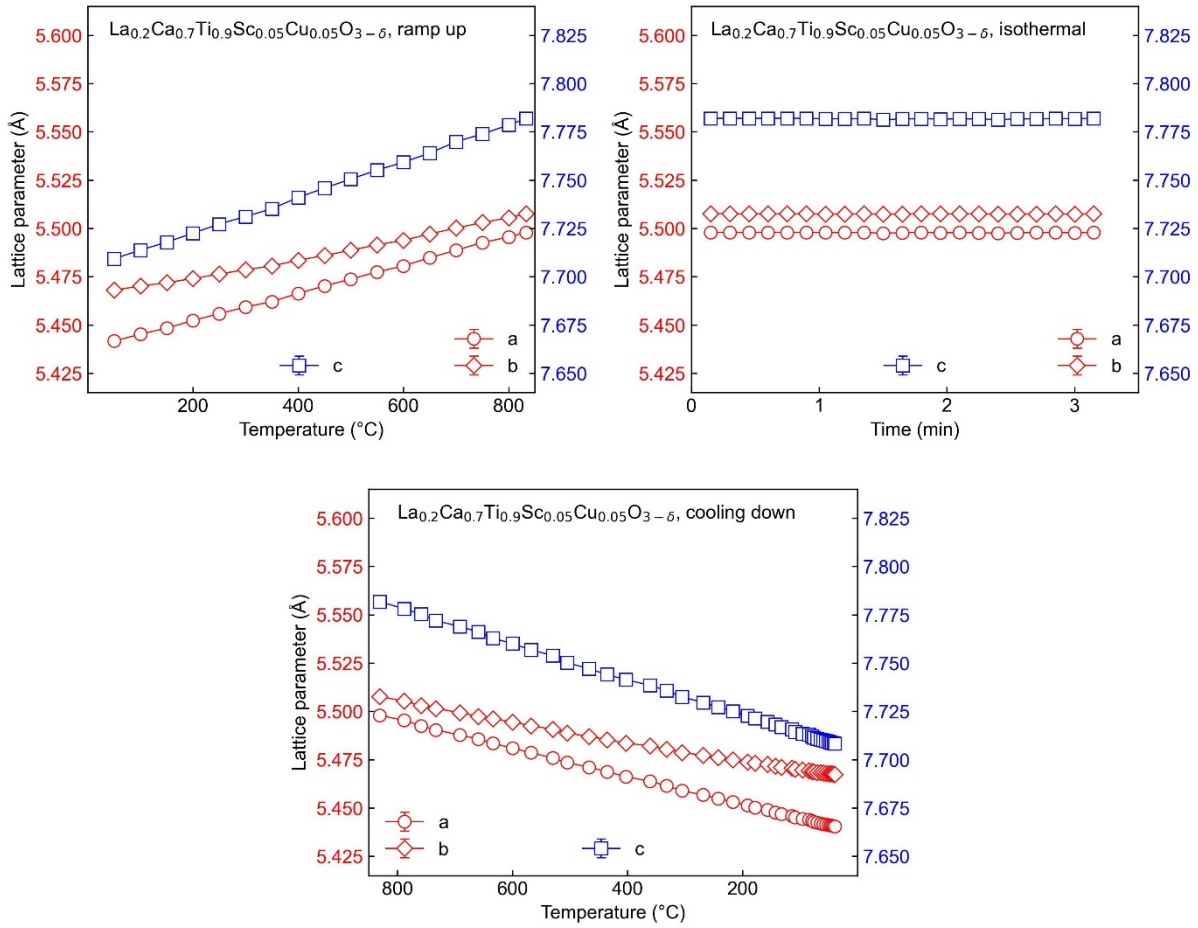

Figure S1.2. Temperature-dependent evolution of lattice parameters upon heating, isothermal dwell, and cooling for $La_{0.2}Ca_{0.7}Ti_{0.9}Sc_{0.05}Cu_{0.05}O_{3-\delta}$.

Estimation of the metal exsolution yield in percent in **Figure 1d** of the manuscript was performed by the exsolution reaction according to Equation (1):

$$La_{0.2}Ca_{0.7}Ti_{0.9}Sc_{0.05}Cu_{0.05}O_{2.925} \rightarrow La_{0.2}Ca_{0.7}Ti_{0.9}Sc_{0.05}Cu_{0.05-x}O_{2.925-x} + xCu(s) + \frac{x}{2}O_2(g) \quad (1)$$

The final weight fraction of the exsolved Cu X_f can be expressed after complete exsolution, i.e., $x = 0.05$, as in Equation (2):

$$X_f = \frac{0.05\ MW_{Cu}}{0.05\ MW_{Cu} + MW_{LCT}} \quad (2)$$

Here, the MW_{LCT} is the molecular weight of the host after exsolution, i.e., without copper and with the corresponding amount of oxygen loss according to Equation 1. The mole fraction of exsolved Cu throughout the in situ experiment was obtained from the weight fraction of Cu obtained from Rietveld refinement (X) relative to the final weight fraction:

$$\frac{x}{0.05} = \frac{X}{X_f} \quad (3)$$

2. Correction of mass loss due to buoyancy and titanium reduction (TGA)

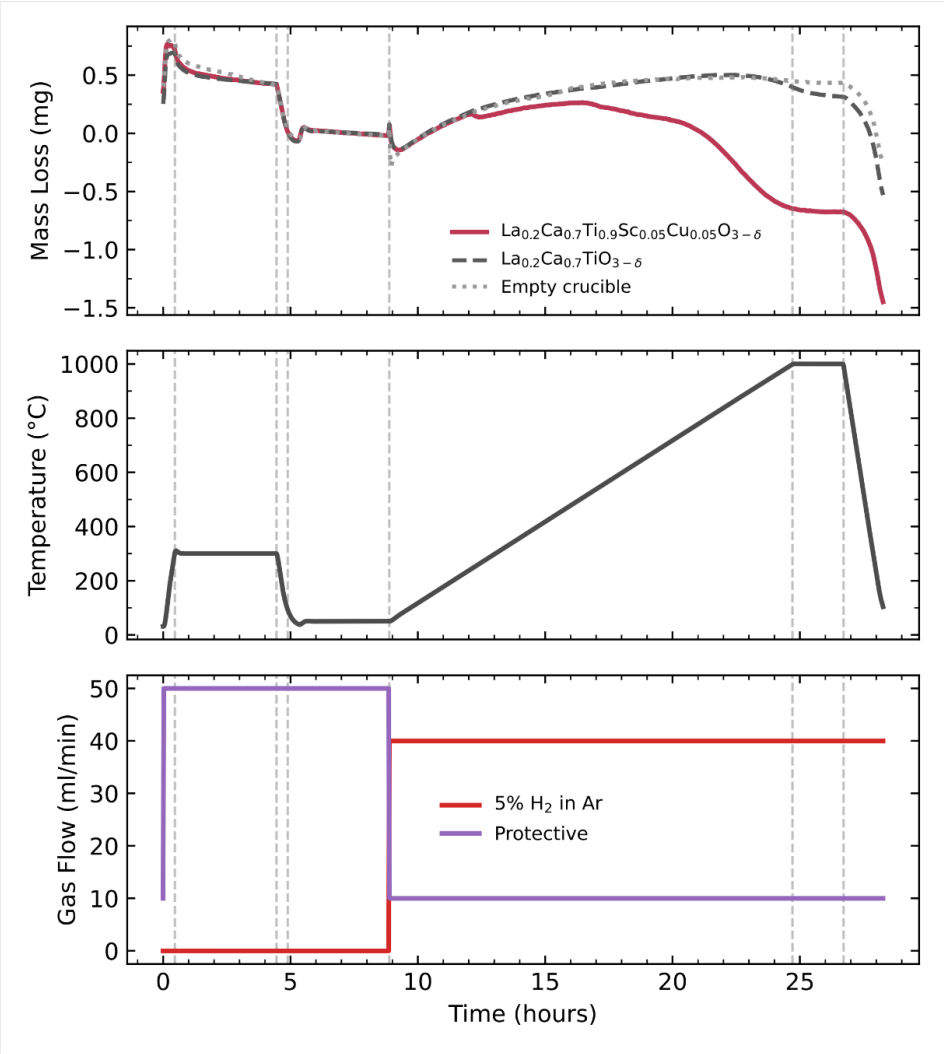

Figure S2.1. Thermogravimetric analysis of $La_{0.2}Ca_{0.7}Ti_{0.9}Sc_{0.05}Cu_{0.05}O_{3-\delta}$ and $La_{0.2}Ca_{0.7}TiO_{3-\delta}$ reference presented in the manuscript visualized by the measured mass loss (top), temperature profile (middle), and gas flow (bottom). Samples of 20-40 µm sized sieved powders (500 mg) were prepared of $La_{0.2}Ca_{0.7}Ti_{0.9}Sc_{0.05}Cu_{0.05}O_{3-\delta}$ (sintered at 1300 °C) and $La_{0.2}Ca_{0.7}TiO_{3-\delta}$.

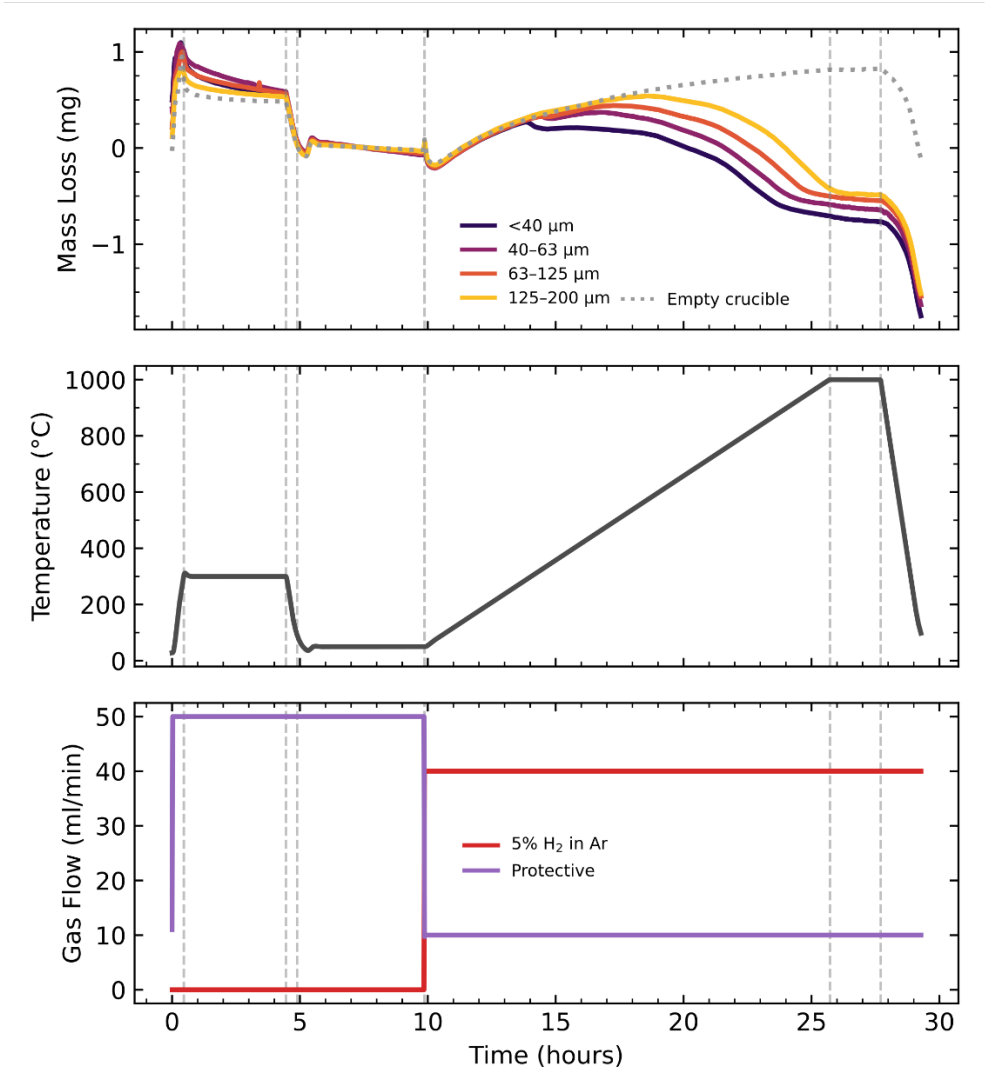

Figure S2.2. Thermogravimetric analysis of $La_{0.2}Ca_{0.7}Ti_{0.9}Sc_{0.05}Cu_{0.05}O_{3-\delta}$ with increasing particle sizes up to 200 µm diameter visualized by the measured mass loss (top), temperature profile (middle), and gas flow (bottom). Samples of sieved powders with diameters of <40 µm, 40–63 µm, 63–125 µm, and 125–200 µm (500 mg) were prepared of $La_{0.2}Ca_{0.7}Ti_{0.9}Sc_{0.05}Cu_{0.05}O_{3-\delta}$ (sintered at 1500 °C). and the $La_{0.2}Ca_{0.7}TiO_{3-\delta}$ reference (20-40 µm).

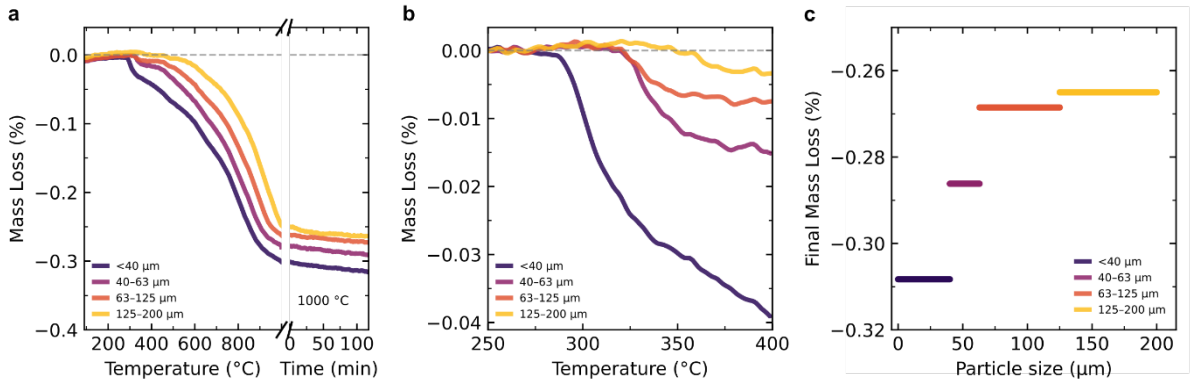

Figure S2.3. Thermogravimetric analysis of $La_{0.2}Ca_{0.7}Ti_{0.9}Sc_{0.05}Cu_{0.05}O_{3-\delta}$ and $La_{0.2}Ca_{0.7}TiO_{3-\delta}$ reference samples with increasing particle sizes up to 200 µm diameters. **a,** Mass loss curves corrected for buoyancy show increased mass loss in the initial stage (approx. 300–350 °C) with increasing surface area. **b**, Magnified region of the onset of the initial stage. **c,** Final mass loss as a function of particle size. The decreased onset temperature with smaller particle sizes may indicate enhanced exsolutionfrom fresh fracture surfaces.

3. Annealing profiles of in situ microscopy experiments (STEM)

Three in-situ STEM experiments were conducted to ensure reproducibility of the findings and evaluate any effects of electron-beam irradiation[1]. Two experiments were conducted on $La_{0.2}Ca_{0.7}Ti_{0.9}Sc_{0.05}Cu_{0.05}O_{3-\delta}$ and one on $La_{0.2}Ca_{0.7}Ti_{0.9}Al_{0.05}Cu_{0.05}O_{3-\delta}$. The employed annealing profiles are presented in **Figure S3.1**. Chronologically, the experiment on $La_{0.2}Ca_{0.7}Ti_{0.9}Al_{0.05}Cu_{0.05}O_{3-\delta}$ was conducted first, aiming to identify the onset temperatures of the stages under the vacuum conditions (10^{-8} mbar). The wedge was monitored during heating at increments of 50 °C. As a result, the onset of the initial, second, and third stage were identified at 400 °C, 600 °C, and 1000 °C, respectively. Lastly, the upper temperature limit of the microchip was evaluated by heating to 1100 °C to monitor particle migration and coalescence. At this temperature, the carbon film and silicon nitride support started degrading and eventually broke after about an hour. The upper temperature limit for the subsequent experiments was therefore set to 1000 °C, sufficient to activate all stages and at which the nanoparticles remain strongly anchored with the microchip remains intact.

The in-situ experiment was repeated for $La_{0.2}Ca_{0.7}Ti_{0.9}Sc_{0.05}Cu_{0.05}O_{3-\delta}$ with the aim of correlating with synchrotron and thermogravimetry experiments. The onset temperature of initial and second stages matched that of the previous experiment. The smallest nanoparticles appeared sensitive to the electron beam when monitored at atomic resolution at 450 °C (**Figure S4.3** g), whereas there were no signs of instability under the electron beam at lower magnification below 600 °C. Further, high magnification imaging was conducted at room temperature after rapid quenching.

Results from the third in-situ experiment is presented in the main text, in which measurements were performed at selected temperatures within the range of each stage. The <110>-wedges of $La_{0.2}Ca_{0.7}Ti_{0.95}Sc_{0.05}Cu_{0.05}O_{3-\delta}$ was studied in the third experiment, while the <111>- and <100>-oriented wedges of $La_{0.2}Ca_{0.7}Ti_{0.95}Sc_{0.05}Cu_{0.05}O_{3-\delta}$ and $La_{0.2}Ca_{0.7}Ti_{0.95}Al_{0.05}Cu_{0.05}O_{3-\delta}$ were studied in the preceding experiment, respectively. All images were taken in STEM with either annular bright-field (ABF)[2] or annular dark-field (ADF) imaging with a low inner collection angle to exploit enhanced contrast from lattice imperfections[3,4].

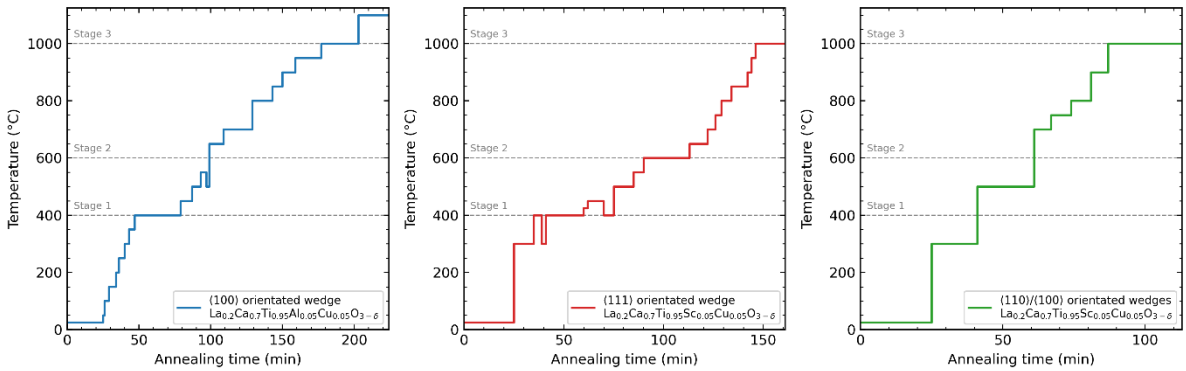

Figure S3.1. Annealing profiles of the in-situ STEM experiments. Annealing temperature and duration for the experiment conducted on $La_{0.2}Ca_{0.7}Ti_{0.9}Al_{0.05}Cu_{0.05}O_{3-\delta}$ (left) and $La_{0.2}Ca_{0.7}Ti_{0.9}Sc_{0.05}Cu_{0.05}O_{3-\delta}$ in the first (middle) and second (right) experiment.

4. Reproduced exsolution at initial stage below 600 °C (STEM)

The pristine wedge together with the first observed and stabilized copper nanoparticles are presented for the wedges in the following order:

- **Figure S4.1**: <110> oriented wedge of $La_{0.2}Ca_{0.7}Ti_{0.9}Sc_{0.05}Cu_{0.05}O_{3-\delta}$
- **Figure S4.2**: <100> oriented wedge of $La_{0.2}Ca_{0.7}Ti_{0.9}Al_{0.05}Cu_{0.05}O_{3-\delta}$
- **Figure S4.3**: <111> oriented wedge of $La_{0.2}Ca_{0.7}Ti_{0.9}Sc_{0.05}Cu_{0.05}O_{3-\delta}$

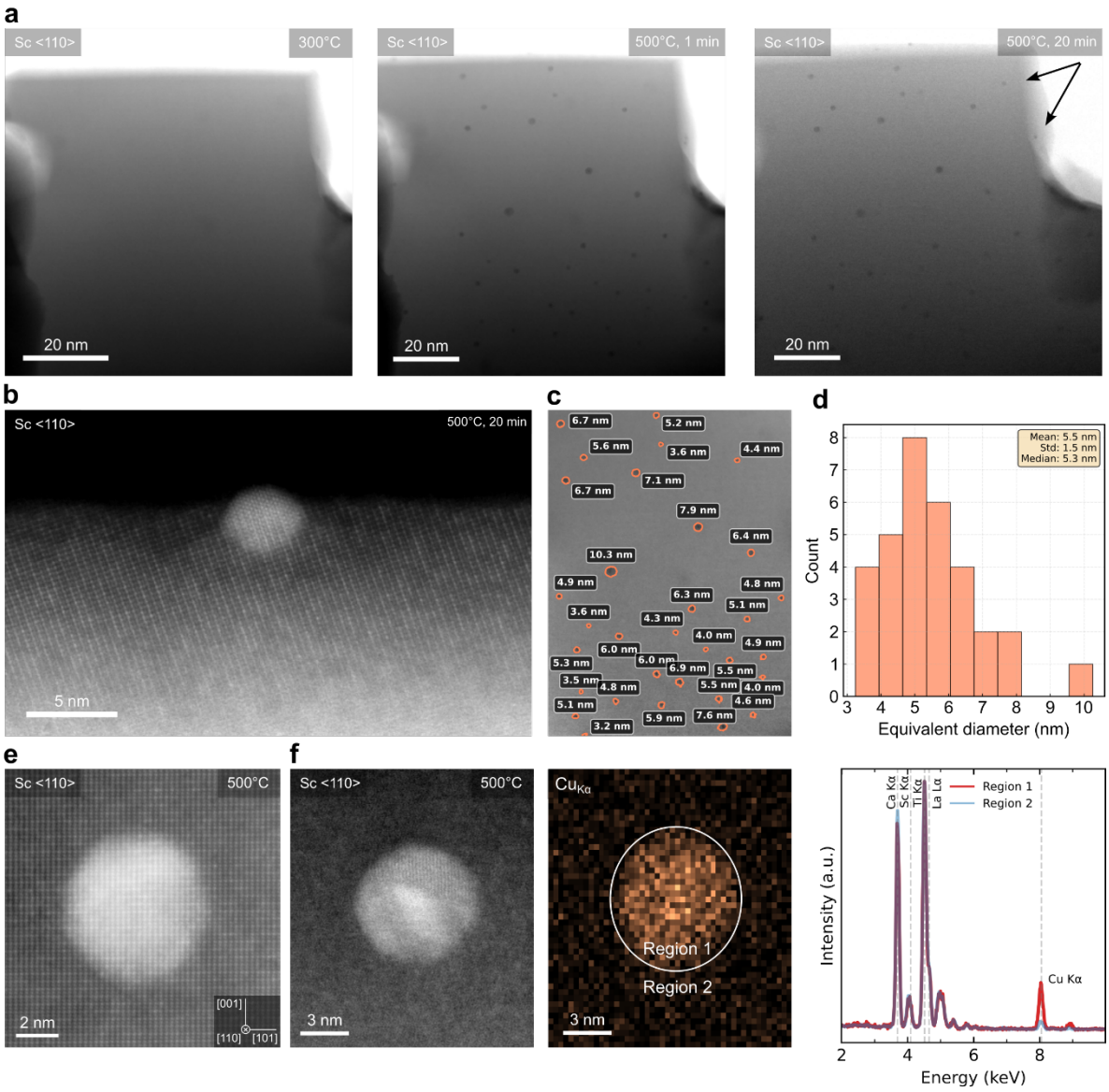

Figure S4.1. Initial exsolution of <110> oriented wedge of $La_{0.2}Ca_{0.7}Ti_{0.9}Sc_{0.05}Cu_{0.05}O_{3-\delta}$. **a,** Overview STEM ABF image of the wedge at 300 °C (left) and at 500 °C after one and twenty minutes (middle, right). The stabilized particle population show no sign of diffusion. Arrows mark two nucleated particles between the observations. **b,** Atomically resolved STEM ADF image of an anchored surface nanoparticle after twenty minutes at 500 °C. **c-d,** Quantified diameters of the nanoparticle population as marked with annotations in the ABF image and presented as a histogram. **e-f,** STEM ADF and energy dispersive X-ray spectroscopy (EDS) elemental map and overlayed spectra of regions 1 and 2 confirm that the exsolved nanoparticles are metallic copper.

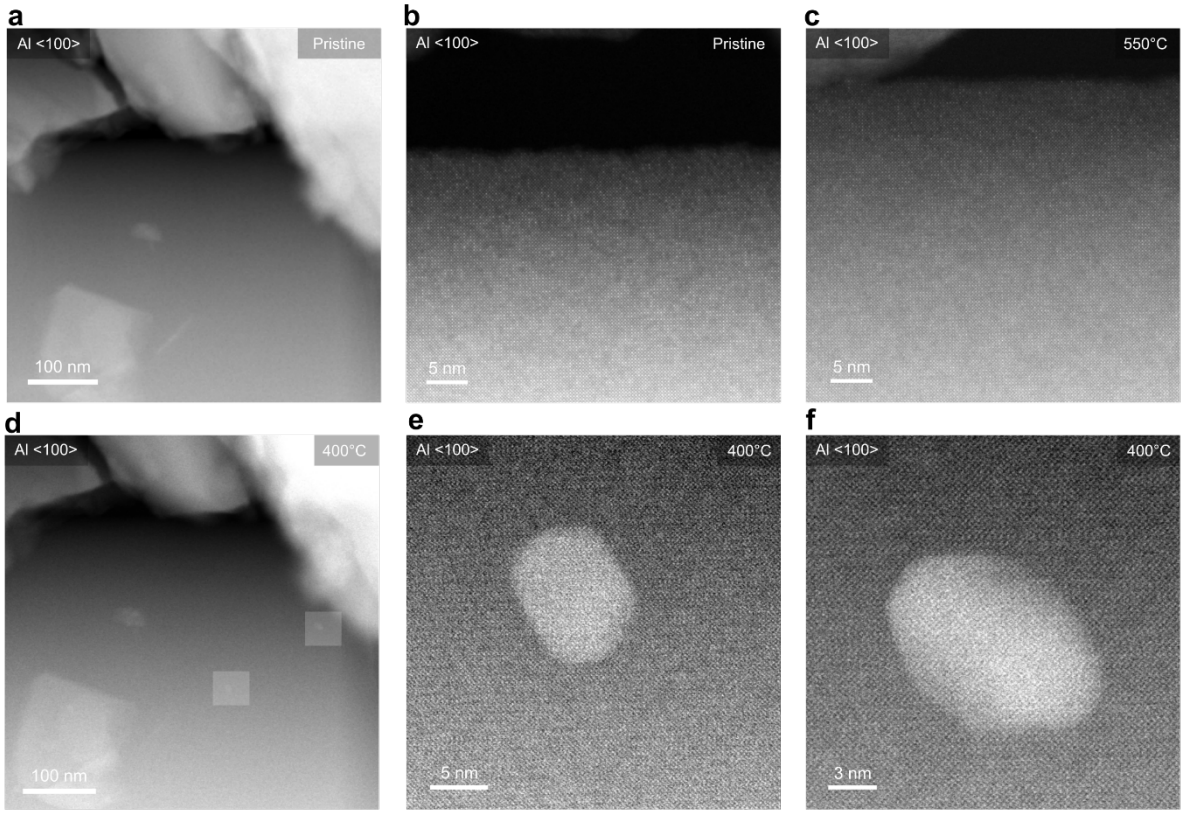

Figure S4.2. Initial exsolution of <100>-oriented wedges of $La_{0.2}Ca_{0.7}Ti_{0.9}Al_{0.05}Cu_{0.05}O_{3-\delta}$. **a,** Overview STEM ADF image of the pristine wedge. **b-c**, Atomically resolved STEM ADF images of the wedge edge at the pristine state and at 550 °C. **d**, Overview STEM-ADF image of the wedge at 400 °C when the surface particles were first observed. **e-f**, Nanoscale STEM ADF image of nanoparticles of varying shapes.

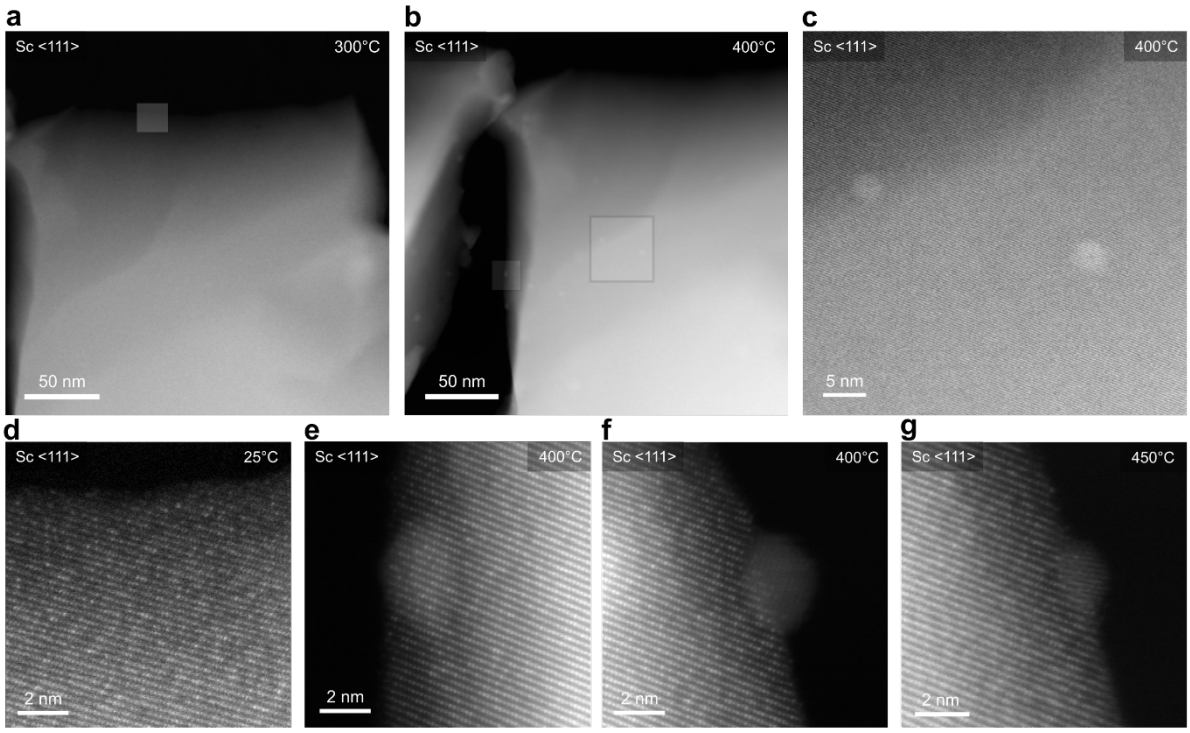

Figure S4.3. Initial exsolution of <111>-oriented wedges of $La_{0.2}Ca_{0.7}Ti_{0.9}Sc_{0.05}Cu_{0.05}O_{3-\delta}$. **a-b,** Overview STEM ADF images of the wedge at 300 °C and 400 °C when particles are first detected. **c,** Nanoscale image of the nanoparticles as marked by the larger square in b. **d,** Atomically resolved STEM-ADF image of the pristine wedge. **e-g,** Atomically resolved STEM-ADF images of surface nanoparticles at 400–450 °C.

5. Reproduced surface reconstruction with endoparticle growth (STEM)

Reconstruction of the perovskite surface forming steps and terraces was similarly observed during the second experiment on the <111>- oriented wedges of $La_{0.2}Ca_{0.7}Ti_{0.9}Sc_{0.05}Cu_{0.05}O_{3-\delta}$. The evolution of the perovskite surface and endoparticle formation is summarized here (**Figure S5.1**). Notably, surface changes seen through the periodic contrast arise prior to the spontaneous collapse.

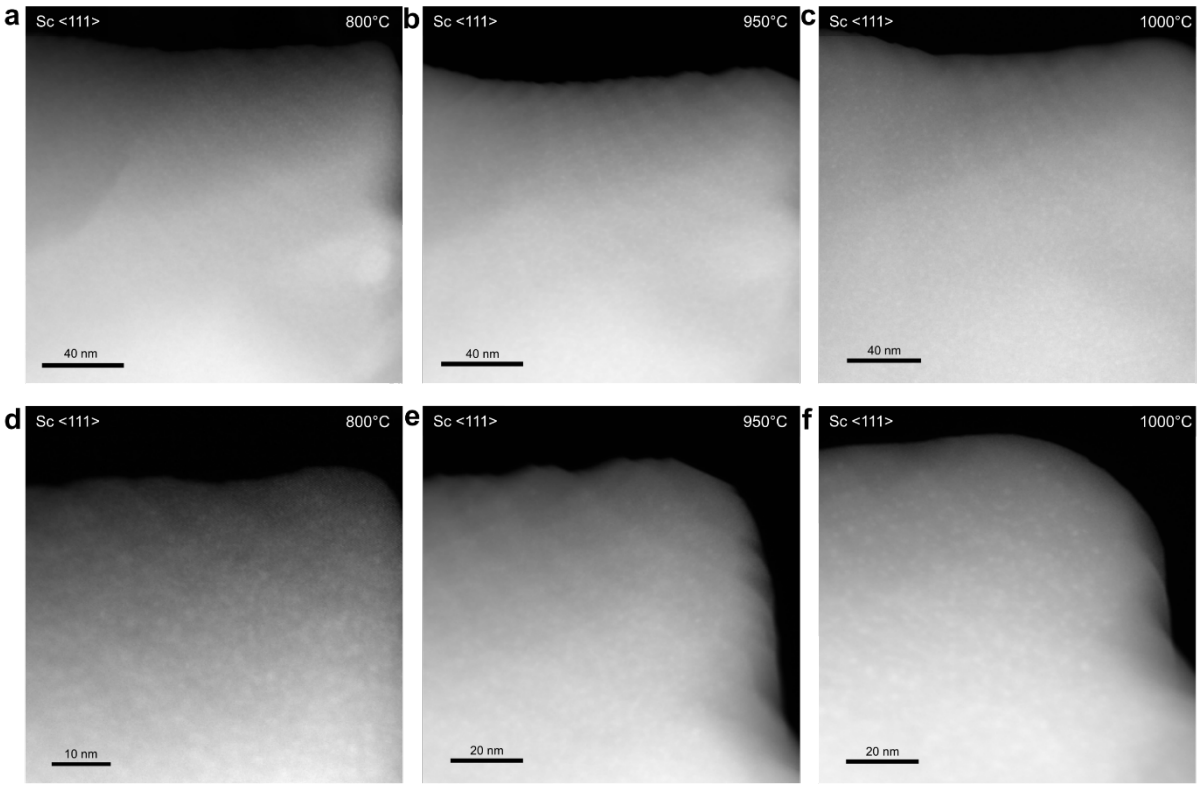

Figure S5.1. Reproduced surface reconstruction with endoparticle growth on <111>- oriented wedge of $La_{0.2}Ca_{0.7}Ti_{0.9}Sc_{0.05}Cu_{0.05}O_{3-\delta}$. **a-c**, Overview STEM-ADF image of the wedge at 800 °C, 950 °C, and 1000 °C show large scale surface transformation concurrent with endoparticle exsolution. **d-f**, STEM-ADF image of the wedge edge show periodic contrast in the perovskite forming at 800 °C, prior to the spontaneous surface reconstruction at 950 °C and later surface smoothening at 1000 °C.

6. Reproduced exsolution observations at 1000 °C (STEM)

The in situ STEM observations for the nanoparticle population observed at 1000 °C when the perovskite surface is smoothed were reproduced for $La_{0.2}Ca_{0.7}Ti_{0.95}Al_{0.05}Cu_{0.05}O_{3-\delta}$ (**Figure S6.1**). Elemental maps representing peak intensity from the model fitting within eXSpy ecosystem of the hyperspy package[5] confirm the ADF contrast correlate to the $Cu_{K\alpha}$ signal (**Figure S6.2**). The elemental maps from the other cations using $Ca_{K\alpha}$, $La_{L\alpha}$, $Ti_{K\alpha}$, and $Sc_{K\alpha}$ show intensity distributions correlated to the thickness of the wedge with minor spatial inhomogeneity that are not correlated to the STEM ADF contrast due to the relatively limited size of the dataset. Migration and coalescence of nanoparticles was observed at 1100 °C at the <100>- oriented wedges of $La_{0.2}Ca_{0.7}Ti_{0.9}Al_{0.05}Cu_{0.05}O_{3-\delta}$ (**Figure S6.3**).

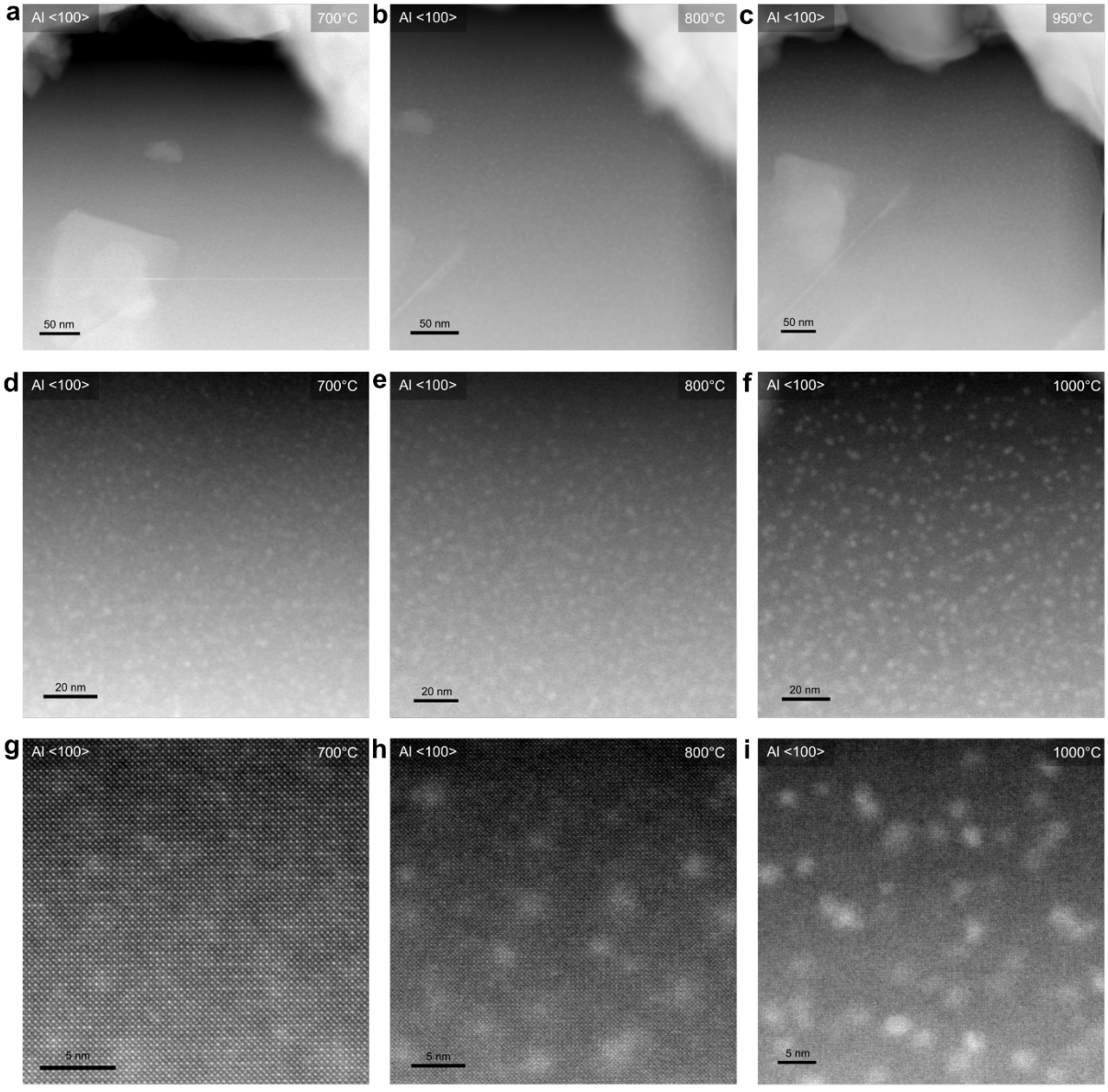

Figure S6.1. Exsolution above 600 °C of <100>- oriented wedges of $La_{0.2}Ca_{0.7}Ti_{0.95}Al_{0.05}Cu_{0.05}O_{3-\delta}$. **a-c,** Low- and **d-f**, high-magnification as well as **g-i**, atomically resolved STEM-ADF image of the wedge at 700 °C, 800 °C, and 950 °C show endoparticle formation and growth. The developing line of contrast is an initial crack in the wedge which become filled by copper particles, and moreover moves into the image as the particle wedge tilts during the experiment.

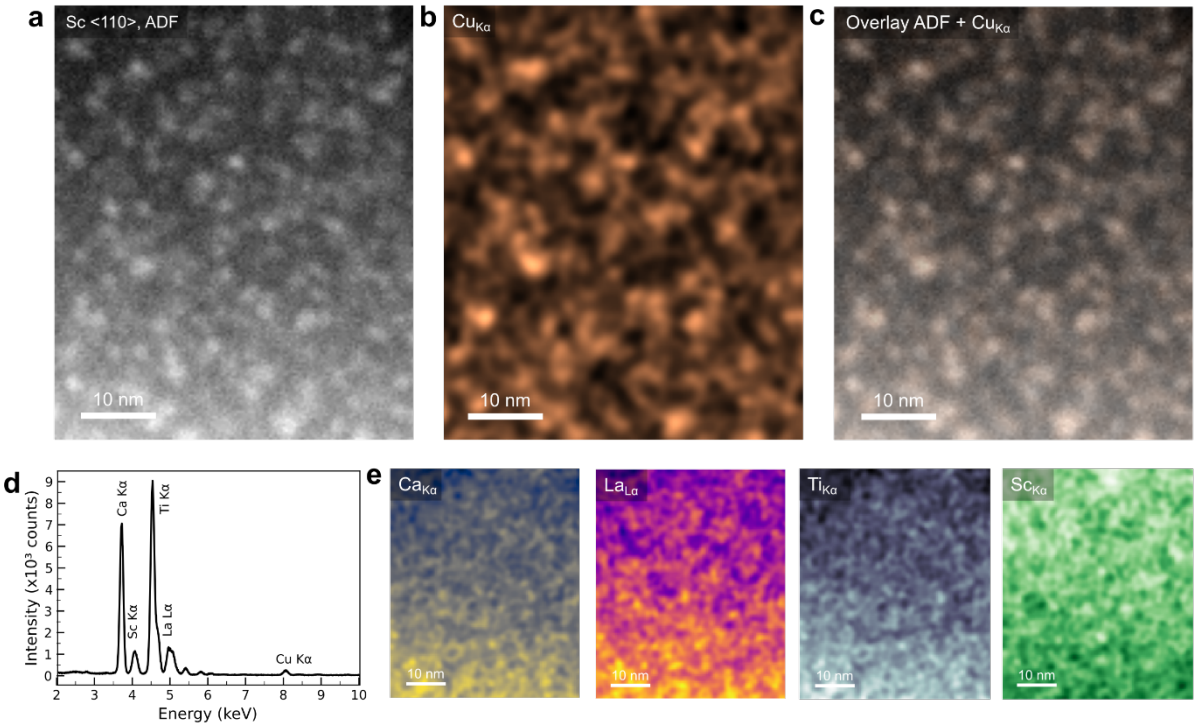

Figure S6.2. STEM energy dispersive spectroscopy analysis of copper population of <110> oriented wedge of $La_{0.2}Ca_{0.7}Ti_{0.95}Sc_{0.05}Cu_{0.05}O_{3-\delta}$ after annealed at 1000 °C. **a,** STEM annular dark field (ADF) image of the exsolved particle population with **b,** elemental map of $Cu_{K\alpha}$ fitting results in the same region. **c,** Strong correlation in the overlayed STEM-ADF image and $Cu_{K\alpha}$ elemental map confirms that the image contrast originates from copper. **d,** Summed EDS spectra show the cation X-ray lines of interest. **e,** Elemental map of $Ca_{K\alpha}$, $La_{L\alpha}$, $Ti_{K\alpha}$, and $Sc_{K\alpha}$.Preprocessing was performed using principal component analysis[6] to remove noise. Gaussian kernel to smooth the signal in nearby pixels was conducted prior to the model fitting to improve signal to noise and background.

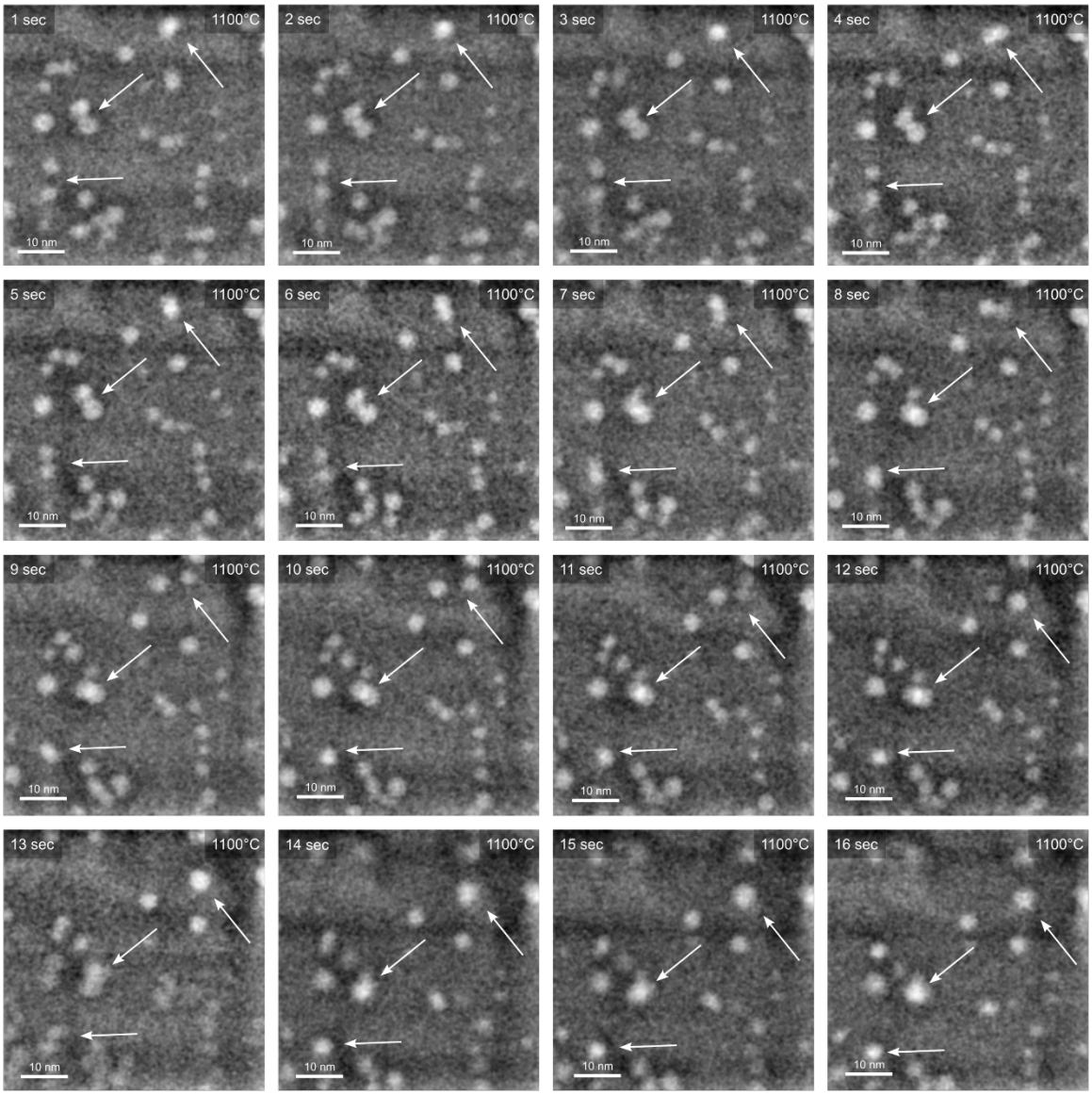

Figure S6.3. Migration and coalescence of surface nanoparticles at 1100 °C of <100>-oriented wedges of $La_{0.2}Ca_{0.7}Ti_{0.9}Al_{0.05}Cu_{0.05}O_{3-\delta}$. 16 second STEM-ADF image series show nanoparticle migration and coalescence as the three examples marked with the arrows. The image series is post-processed using adaptive histogram equivalence to enhance contrast, a low pass Fourier filter to remove noise, and a Gaussian filter to smooth the image by the use of the SciPy package[7].

References

1. Sarkar, R., Rentenberger, C. & Rajagopalan, J. Electron Beam Induced Artifacts During in situ TEM Deformation of Nanostructured Metals. *Sci Rep* **5**, 16345 (2015).
2. Findlay, S. D. *et al.* Dynamics of annular bright field imaging in scanning transmission electron microscopy. *Ultramicroscopy* **110**, 903–923 (2010).
3. Phillips, P. J. *et al.* Atomic-resolution defect contrast in low angle annular dark-field STEM. *Ultramicroscopy* **116**, 47–55 (2012).
4. Muller, D. A., Nakagawa, N., Ohtomo, A., Grazul, J. L. & Hwang, H. Y. Atomic-scale imaging of nanoengineered oxygen vacancy profiles in SrTiO3. *Nature* **430**, 657–661 (2004).
5. Peña, F. de la *et al.* hyperspy/hyperspy: v2.2.0. Zenodo https://doi.org/10.5281/zenodo.14057415 (2024).
6. Greenacre, M. *et al.* Principal component analysis. *Nat Rev Methods Primers* **2**, 100 (2022).
7. Virtanen, P. *et al.* SciPy 1.0: fundamental algorithms for scientific computing in Python. *Nat Methods* **17**, 261–272 (2020).